# Ensemble Kalman Filter Analyses of the 29–30 May 2004 Oklahoma Tornadic Thunderstorm Using One- and Two-Moment Bulk Microphysics Schemes, with Verification against Polarimetric Radar Data

YOUNGSUN JUNG

*Center for Analysis and Prediction of Storms, University of Oklahoma, Norman, Oklahoma*

MING XUE

*Center for Analysis and Prediction of Storms, and School of Meteorology, University of Oklahoma, Norman, Oklahoma*

MINGJING TONG*

*Center for Analysis and Prediction of Storms, University of Oklahoma, Norman, Oklahoma*

(Manuscript received 7 February 2011, in final form 8 December 2011)

ABSTRACT

The performance of ensemble Kalman filter (EnKF) analysis is investigated for the tornadic supercell on 29–30 May 2004 in Oklahoma using a dual-moment (DM) bulk microphysics scheme in the Advanced Regional Prediction System (ARPS) model. The comparison of results using single-moment (SM) and DM microphysics schemes evaluates the benefits of using one over the other during storm analysis. Observations from a single operational Weather Surveillance Radar-1988 Doppler (WSR-88D) are assimilated and a polarimetric WSR-88D in Norman, Oklahoma (KOUN), is used to assess the quality of the analysis.

Analyzed reflectivity and radial velocity in the SM and DM experiments compare favorably with independent radar observations in general. However, simulated polarimetric signatures obtained from analyses using a DM scheme agree significantly better with polarimetric signatures observed by KOUN in terms of the general structure, location, and intensity of the signatures than those generated from analyses using an SM scheme.

These results demonstrate for the first time for a real supercell storm that EnKF data assimilation using a numerical model with an adequate microphysics scheme (i.e., a scheme that predicts at least two moments of the hydrometeor size distributions) is capable of producing polarimetric radar signatures similar to those seen in observations without directly assimilating polarimetric data. In such cases, the polarimetric data also serve as completely independent observations for the verification purposes.

## 1. Introduction

Microphysical processes within clouds strongly influence the evolution of convective systems, yet many complex microphysical processes and their effects are not fully understood. In numerical weather prediction (NWP) models, processes associated with the initiation, growth, breakup, evaporation, and fallout of precipitation particles, as well as many other processes, are parameterized using bin (spectral) or bulk parameterization schemes. Because of the complexity and incomplete understanding of these processes, many uncertainties exist in their parameterization. For real-time NWP models including microphysical parameterization, bulk microphysical parameterization (BMP) is exclusively used over bin schemes to limit computational cost.

BMP schemes are based on a gross representation of particle size distributions (PSDs) for each hydrometeor species, whereas bin schemes attempt to represent PSDs explicitly. In BMP schemes, PSDs are assumed to have

* Current affiliation: National Centers for Environmental Prediction, Camp Springs, Maryland.

*Corresponding author address:* Youngsun Jung, Center for Analysis and Prediction of Storms, National Weather Center, Suite 4226, 120 David L. Boren Blvd., Norman, OK 73072.
E-mail: youngsun.jung@ou.edu

DOI: 10.1175/MWR-D-11-00032.1

© 2012 American Meteorological Society

a specified functional form. A well-known functional form based on observed rain drop size distributions (DSDs) is a generalized gamma distribution (e.g., Ulbrich 1983; Milbrandt and Yau 2005a),

$$N_x(D) = N_{0x} D^{\alpha_x} e^{-\lambda_x D}, \quad (1)$$

which has three free parameters: the intercept parameter $N_0$, the shape parameter $\alpha$, and the slope parameter $\lambda$. In this equation, $N(D)$ is the number density as a function of particle diameter $D$ and subscript $x$ refers to one of the hydrometeor species. Single-moment (SM) BMP schemes typically fix $N_0$, set $\alpha = 0$, and predict $\lambda$, which is a function of the mass content that is directly predicted (e.g., Lin et al. 1983; Cotton et al. 1986). Many dual-moment (DM) BMP schemes predict mass content and total number concentration allowing $N_0$ and $\lambda$ to vary while holding $\alpha$ constant (e.g., Ziegler 1985; Ferrier 1994; Meyers et al. 1997; Milbrandt and Yau 2005a,b). It is also possible to predict $\alpha$ as an additional free parameter by predicting an additional moment, such as the radar reflectivity factor (the 6th moment of the PSD). Schemes that treat $\alpha$ in this manner are called three-moment (TM) schemes (e.g., Milbrandt and Yau 2005b). Because each free parameter requires a prognostic equation for each microphysical species, computational costs increase significantly when moving to a multimoment (MM) BMP scheme.

In recent decades, a rapid increase in computing power has motivated efforts to improve BMP schemes by adding more hydrometeor species, including more microphysical processes, and/or predicting more free PSD parameters (e.g., Ferrier 1994; Ferrier et al. 1995; Milbrandt and Yau 2005a,b; Morrison et al. 2005; Koenig and Murray 1976). Studies have shown that schemes allowing two and three independently varying PSD parameters produce simulated convective storms that are more consistent with observations than SM schemes that predict only one free parameter; the largest improvement is often found when moving from an SM to a DM scheme, although improvement has also been noted when moving from a DM to a TM scheme (Milbrandt and Yau 2006; Jung et al. 2010, hereafter JXZ10; Dawson et al. 2010). In these studies, supercell thunderstorms simulated using a multimoment microphysics scheme showed a more realistic reflectivity structure, particularly in the forward-flank region, and more realistic cold pool strength. Because the DM scheme predicts the total mass and the total number concentration independently, it is capable of simulating drop growth (shrinking) during accretion or diffusion (evaporation) while keeping the number concentration constant, or the number concentration changes during aggregation or breakup while the total mass remains constant. More importantly, the DM scheme allows size sorting because of differential sedimentation that results in larger mean sizes at lower levels than at upper levels. Those processes cannot be simulated with an SM scheme because the total mass and the total number concentration are always monotonically related. For more details, the reader is referred to Milbrandt and Yau (2005a).

Whereas the studies mentioned above suggest that a DM scheme may simulate storms more realistically than an SM scheme, initializing model states when using a DM scheme poses additional challenges. Convective-scale state estimation is severely underconstrained by observations, even when using radar data. Because the DM scheme doubles the number of microphysical variables compared to the SM scheme, the problem becomes more challenging, as the DM scheme significantly increases the number of state variables to be estimated while relying on the same number of observations. Xue et al. (2010, hereafter XJZ10) found slower error reduction rates during data assimilation (DA) cycles when both the truth simulation and the corresponding observing system simulation experiments (OSSEs) used a DM scheme as compared to an SM scheme using its own truth simulation and the corresponding OSSEs.

In recent years, the ensemble Kalman filter (EnKF) has enjoyed encouraging success in meteorological data assimilation from global to convective scales (Evensen 1994; Evensen and Leeuwen 1996; Burgers et al. 1998; Houtekamer and Mitchell 1998; Anderson 2001; Bishop et al. 2001; Whitaker and Hamill 2002; Evensen 2003; Tippett et al. 2003; Snyder and Zhang 2003; Dowell et al. 2004; Tong and Xue 2005, hereafter TX05; Xue et al. 2006, hereafter XTD06; Jung et al. 2008b, hereafter JXZS08; Dowell et al. 2011; Dawson et al. 2012). The EnKF method is especially useful at the convective scale because no adjoint model is needed for the complex and highly nonlinear microphysical processes that occur at convective scales. XJZ10 demonstrated the capability of an EnKF system to estimate multiple moments of PSDs with simulated single-polarization Doppler radar observations.

In XJZ10, the Advanced Regional Prediction System (ARPS) EnKF system was able to estimate all state variables associated with the Milbrandt and Yau (2005a) DM scheme reasonably well when both reflectivity and radial velocity were assimilated either in a perfect model scenario or in the presence of certain model errors. However, XJZ10 suggested that the same level of performance may not be achieved when significant model and/or other sources of error exist. When a problem is significantly underconstrained by observations, the large model error may limit the ability of the filter to develop

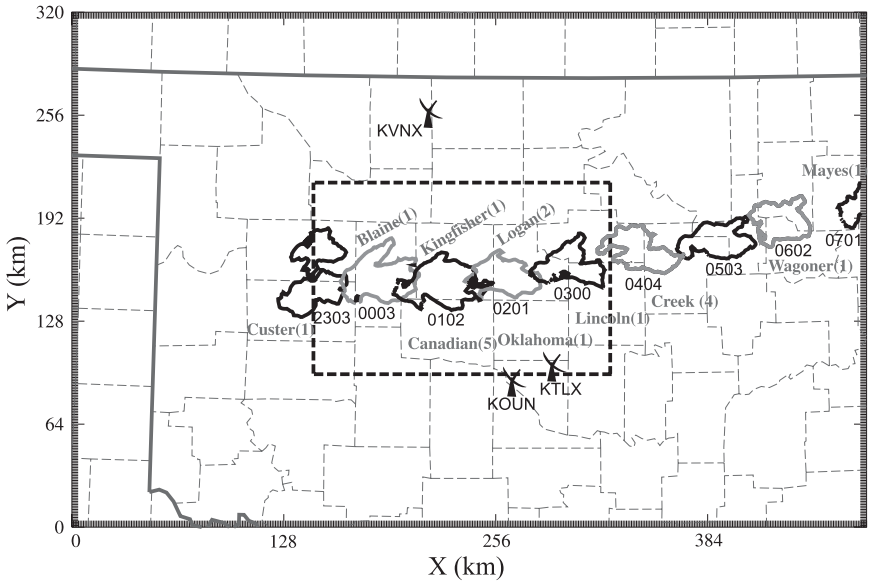


FIG. 1. Reflectivity greater than 40 dB$Z$ at 0.5° of KTLX (thick solid contours) between 2303 UTC 29 May and 0701 UTC 30 May 2004. The location of KTLX is marked with a radar symbol. The thick dashed rectangle denotes the analysis domain. The number of tornadoes by county associated with this storm is shown in the parentheses next to the county names.

reliable multivariate covariance, leading to filter divergence. Much research is still required to determine the ability of an EnKF system to estimate all state variables necessary to initialize a multimoment microphysics scheme using real data.

The primary goal of this paper is to demonstrate, for the first time in a real data case, that the EnKF DA method is able to estimate model states associated with a two-moment microphysics scheme (i.e., both mixing ratios and total number concentrations) and that the estimated states can provide simulated polarimetric radar signatures that match real radar observations. With an SM scheme, the system is fundamentally incapable of simulating such signatures, as shown in JXZ10 with simulated data. An enhanced version of the XJZ10 EnKF DA system with a DM scheme is applied to a real tornadic supercell storm case. Specifically, we select the tornado outbreak that occurred on 29–30 May 2004 in central Oklahoma. Analyses using SM and DM microphysics schemes are directly compared. For a more stringent comparison, we assimilate observations from only one Weather Surveillance Radar-1988 Doppler (WSR-88D) while using observations from both another operational WSR-88D and a research polarimetric radar for independent verification.

The rest of this paper is organized as follows: a brief overview of the tornado outbreak case is first given in section 2. In section 3, we briefly describe the forecast model, EnKF assimilation system, and design of our experiments. We also introduce the radar observations used for data assimilation and verification. We discuss the assimilation results obtained using DM and SM schemes and verify them against radar observations in section 4. Finally, section 5 includes a summary and conclusions.

## 2. Overview of the 29–30 May 2004 tornado outbreak

During the late afternoon and evening of 29 May 2004 an enduring supercell thunderstorm traversed central Oklahoma, spawning 18 tornadoes. The storm lasted for nearly 12 h, during which time it traveled almost 300 miles from western Oklahoma to the Oklahoma–Arkansas border (Fig. 1). Briefly, an upper-level low pressure system moved out of the Rockies into the southern plains on the afternoon of 29 May (not shown). A dryline developed in the southern plains, passing through the central Panhandle area in the early morning of 29 May, and moved into far western Oklahoma by 0000 UTC 30 May. By this time, a surface front had advanced from Colorado into western Oklahoma, catching up to the dryline in Kansas. The convective available potential energy (CAPE) in the 0000 UTC 30 May Norman, Oklahoma, sounding was moderate (2344 J kg$^{-1}$) and convective inhibition (CIN) was relatively low ($-62$ J kg$^{-1}$).

By early afternoon, several convective storms formed along the dryline near the western border of Oklahoma and quickly moved northeastward. A few smaller storms at the southern end of a line of storms merged and grew into a strong supercell storm by 2300 UTC in western

central Oklahoma (Fig. 1). This supercell storm produced a number of tornadoes, large destructive hail, and damaging winds as it moved eastward.

This case garnered the attention of a number of studies, some still ongoing, because it occurred during the Thunderstorm Electrification and Lightning Experiment (TEKEX; MacGorman et al. 2008). Bluestein et al. (2007) and Kumjian and Ryzhkov (2008) examined specific polarimetric signatures during the mature stage of the storm based on radar observations. Hu (2005) and Tong (2006) attempted to analyze and predict this storm using three-dimensional variational data assimilation (3DVAR) and EnKF, respectively. Hu (2005) noticed the significant position error of the storm during the assimilation and forecasting process and attempted to introduce a phase-correction procedure to reduce this error. The results of Tong (2006) using data from one or two WSR-88Ds and an SM scheme showed a good fit between and the analyses and observations. Nevertheless, forecasts that started from the final analyses deteriorated quickly. Tong (2006) speculated that model errors, most likely those associated with microphysics and resolution, were responsible for the large forecast errors. Some aspects of the analyses were not verified because of the lack of direct observations. More detailed descriptions of the storm initiation, evolution, and associated tornadoes of the event can be found in Hu (2005).

## 3. Experiment design

### *a. Prediction model*

Predictions during the EnKF cycles are performed using the Advanced Regional Prediction System (Xue et al. 2000; 2001; 2003), which is a fully compressible, nonhydrostatic atmospheric model. ARPS predicts the three velocity components $u$, $v$, and $w$, potential temperature $\theta$, pressure $p$, water vapor mixing ratio $q_v$, as well as microphysical state variables. Microphysical variables may include mixing ratios of cloud water, rainwater, ice, snow, and graupel and/or hail ($q_c$, $q_r$, $q_i$, $q_s$, $q_g$, and/or $q_h$, respectively), their total number concentrations ($N_{tc}$, $N_{tr}$, $N_{ti}$, $N_{ts}$, $N_{tg}$, and/or $N_{th}$), and reflectivity factor ($Z_{tr}$, $Z_{ti}$, $Z_{ts}$, $Z_{tg}$, and/or $Z_{th}$) depending on the number of moments predicted by the selected microphysics scheme. In this study, the double-moment microphysics schemes of Milbrandt and Yau (2005a,b; MY scheme) are used for our comparison study. For a single-moment microphysics scheme, the commonly used Lin et al. (1983) scheme was employed. The intercept parameter values for rain, snow, and hail size distributions used in this study are $8.0 \times 10^5$ m$^{-4}$, $3.0 \times 10^6$ m$^{-4}$, and $4.0 \times 10^4$ m$^{-4}$, respectively. Here, the rain intercept parameter was reduced from the default $8.0 \times 10^6$ m$^{-4}$ following Snook and Xue (2008).

The basic EnKF configurations are largely inherited from the OSSEs described in XJZ10. The particle size distributions for all categories are assumed to be exponential for SM and DM schemes; shape parameters in the gamma PSDs are set to zero in the forward observation operator. The graupel category is turned off for the DM scheme as was done in XJZ10. Turning off graupel has two primary advantages. First, it may alleviate the tendency of microphysics schemes to overpredict graupel–hail in the supercell storm simulation (Milbrandt and Yau 2006). Second, the DM scheme doubles the number of microphysical variables predicted, inevitably leading to increased uncertainty in the analysis, as discussed earlier. By turning off graupel, we reduce the number of microphysical-state variables. Our test experiments with idealized supercell simulations show that eliminating graupel does not significantly impact storm evolution.

An analysis domain measuring $180 \times 120 \times 16$ km$^3$ is used with a horizontal grid spacing of 1 km and 40 vertical levels. Vertical grid stretching is applied such that the vertical spacing varies from 100 m at the surface to 700 m at the model top. Full model physics are used, including the National Aeronautics and Space Administration (NASA) Goddard Space Flight Center (GSFC) longwave and shortwave radiation parameterization, stability-dependent surface-layer physics, a two-layer soil model initialized with the National Centers for Environmental Prediction (NCEP) Eta Model analysis, and 1.5-order turbulent kinetic energy (TKE)-based subgrid-scale turbulence parameterization (see Xue et al. 2001 for details). Although TKE and soil variables are predicted, they are not updated, as in our earlier OSSE studies. Updating soil variables will require future research.

External ensemble boundary conditions are created using the scaled lagged average forecasting (SLAF) technique (Ebisuzaki and Kalnay 1991; Hou et al. 2001; Kong et al. 2006). First, the Eta Model analyses at 1800 UTC 19 May and 0000 UTC 30 May are interpolated in time and space to a 3-km horizontal resolution grid at hourly intervals. The area of the 3-km grid is 900 km $\times$ 900 km (not shown). Next, ARPS 3DVAR analyses are performed using the interpolated Eta grids as a background and all available rawinsondes and surface observations, including those from the Oklahoma Mesonet, at hourly intervals. ARPS forecasts are then initiated from these analyses and run until 0000 UTC 30 May. Various combinations of these forecasts and the analysis valid at 0000 UTC are utilized to create 60 initial conditions. Finally, ensemble

forecasts on the 3-km grid are launched starting from the ensemble initial conditions and run until 0100 UTC. Ensemble boundary conditions for ensemble analyses over the assimilation window are produced using these ensemble forecasts. The 3-km initial conditions at 0000 UTC provide the initial background ensemble and the 3-km ensemble forecasts supply perturbed boundary conditions for the 1-km EnKF analyses.

### b. Data assimilation procedure

The fundamental configuration of the EnKF analysis is adopted from JXZS08 and XJZ10. Model-state variables are estimated using an ensemble square root filter (EnSRF) algorithm based on that of Whitaker and Hamill (2002). A full description of the square root filter and its implementation in the ARPS EnKF system can be found in XTD06. The forward observation operator developed in Jung et al. (2008a, hereafter JZX08) and modified in XJZ10 the total number concentrations available with the DM scheme is used to assimilate radar reflectivity ($Z_H$, where $H$ is horizontal polarization) and radial velocity ($V_r$) collected by the Oklahoma City, Oklahoma, WSR-88D (KTLX). Briefly, the scattering amplitudes of rain computed using T-matrix codes (Waterman 1969; Vivekanandan et al. 1991) at a uniform drop size interval are fitted to a power-law function of the drop size for reflectivity. For ice, the Rayleigh scattering approximation is utilized. The presence of wet snow and wet hail in the melting layer is accounted for by defining a water fraction in the melting snow or hail. This melting ice model allows for continuously varying density and dielectric constants throughout the melting process. For radial velocity, the forward observation operator for radial velocity defined in XTD06 is used.

A 60-member ensemble is initialized on the 1-km grid at 0000 UTC 30 May by adding spatially correlated perturbations to the initial conditions interpolated from the 3-km ensemble forecasts described in section 3a. A two-dimensional (2D) recursive filter (Purser et al. 2003; Barker et al. 2003) is applied horizontally with a decorrelation length scale of 6 km, and a homogeneous Gaussian filter (Huang 2000; Liu and Xue 2006) with a length scale of 3 km is applied vertically to three-dimensional (3D) fields with random Gaussian distributed perturbations to generate smoothed, spatially correlated initial perturbations. The standard deviations of the final perturbations added to each variable are 2 m s$^{-1}$ for $u$, $v$, and $w$; 1 K for $\theta$; and 0.2 g kg$^{-1}$ for the mixing ratios of hydrometeors ($q_v$, $q_c$, $q_r$, $q_i$, $q_s$, and $q_h$). Only positive perturbations are produced for $\theta$, $q_v$, $q_c$, $q_r$, $q_i$, $q_s$, and $q_h$. Perturbations are added to $u$, $v$, and $\theta$ in the entire domain and to $w$ and mixing ratios $q_v$, $q_c$, $q_r$, $q_i$, $q_s$, and $q_h$ at grid points located within 4 km horizontally and 2 km vertically of significant observed reflectivity (where $Z_H$ exceeds 30 dB$Z$). At the initial time in this experiment, the number concentrations were diagnosed using the perturbed mixing ratios and their default intercept parameters, using the DM scheme to maintain a degree of consistency with mixing ratios. In this way, $N_t$ is guaranteed to be nonzero when $q$ is nonzero. If instead both $q$ and $N_t$ had been perturbed independently, some combinations could have occasionally been assigned values that would lead to instability. As an example, the initial state of select fields in ensemble member 1 is shown in Fig. 2.

During the forecast, the shape parameters of the gamma PSDs for rain and hail are perturbed as an ensemble as in XJZ10 for both SM and DM experiments. The shape parameter for rain varies from 0 to 3, while that of hail changes from 3 to 0 sequentially—both at constant intervals of 0.05—giving rise to 60 values that are used in the ensemble.

The cutoff radius used in the covariance localization function (Gaspari and Cohn 1999) is set to 6 km in all directions. A multiplicative inflation (Anderson 2001; TX05) factor of 15% is applied to all model states except number concentrations because inflating the number concentration can sometimes have a negative impact on the filter performance in the early cycles because of their large dynamic ranges and large spreads. Filter divergence due to underdispersion is typically much more serious in real data experiments. Similar to Dowell and Wicker (2009), additive noise is found to help maintain ensemble spread during data assimilation. We apply additive noise every 5 min during a 55-min data assimilation window. Again, a 2D recursive filter and a homogeneous Gaussian filter are used to produce smoothed additive noise, but with a 12-km length scale in both the horizontal and the vertical directions; small length scales were found to produce worse results with a DM scheme and cause forecast instability in some members.

Additive noise is added only to $u$, $v$, and $\theta$, with their standard deviations being 0.5 m s$^{-1}$, 0.5 m s$^{-1}$, and 0.5 K, respectively, for the SM experiment (EXP_SM) and 0.75 m s$^{-1}$, 0.75 m s$^{-1}$, and 0.75, respectively, for the experiment using a DM scheme (EXP_DM). We observed faster spread reduction in EXP_DM and, consequently, decided to use more additive noise. In this study, the additive noise is added everywhere. It is found that the noise added upstream of the storm helps to maintain the spread within the storm but can lead to too large a spread downstream of the storm where the spread is already quite large. For the purpose of this study, the spread downstream of the storm is of less concern. Overall, we found that adding the noise everywhere worked better for this case, and our assimilation of reflectivity data everywhere, as was first found

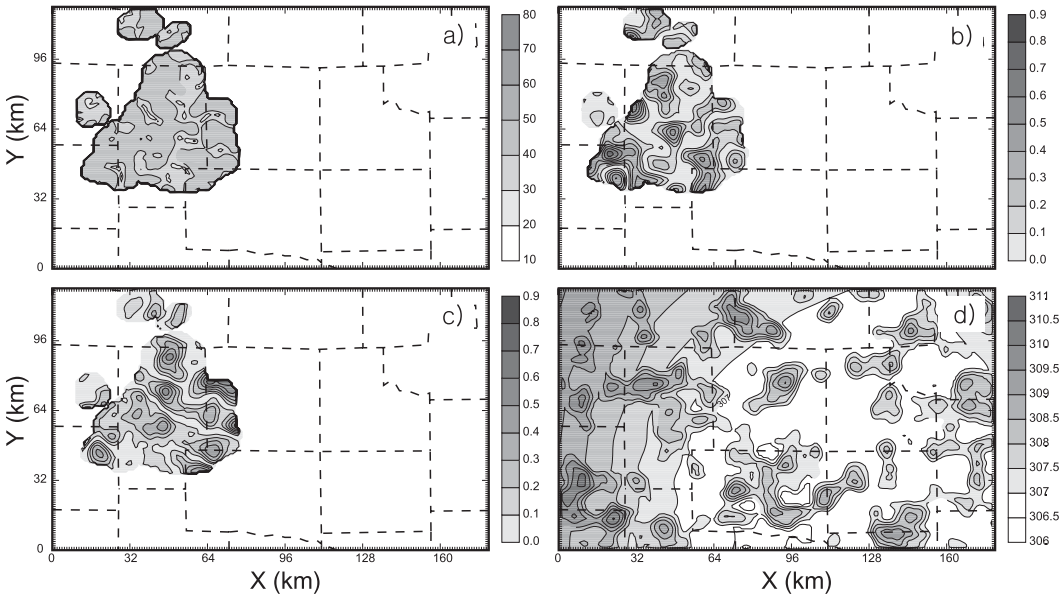


FIG. 2. Initial fields of ensemble member 1 for (a) reflectivity (dB$Z$), (b) rainwater mixing ratio (g kg$^{-1}$), (c) hail mixing ratio (g kg$^{-1}$), and (d) potential temperature (K) after the perturbations are added at $z = 2$ km MSL.

in TX05, helps to suppress spurious storms that may develop out of the noise. XJZ10 showed that perturbing the shape parameter of gamma PSDs of rain and hail within the forecast ensemble, as previously described, helped improve PSD state estimation. The above inflation configurations were found to produce the best results after numerous experiments.

The assimilation of KTLX data on the 1-km grid starts at 0005 UTC 30 May. It is performed every 5 min until 0100 UTC. Reflectivity data from the entire domain and $V_r$ from regions where observed reflectivity is greater than 5 dB$Z$ are assimilated. As in TX05, the assimilation of reflectivity data in nonprecipitation regions is found to help suppress the spurious convection that may develop in the model. All state variables, except pressure, are updated when analyzing either $Z_H$ or $V_r$ data. Observation errors in the filter are assumed to be 3 dB$Z$ for $Z_H$ and 2 m s$^{-1}$ for $V_r$.

### c. Radar observations

As previously mentioned, radar reflectivity and radial velocity data ($Z_H$ and $V_r$) from the Oklahoma City radar are assimilated. The WSR-88D at Vance Air Force Base (KVNX), which is located in northwestern Oklahoma, also provided coverage of the storm. These data and data from the polarimetric WSR-88D located in Norman (KOUN) are used for independent verification.

Verification of analyzed thunderstorms represents a major challenge because most state variables are not directly observed. XJZ10 and JXZ10 showed that reflectivity alone is insufficient for determining the quality of estimated microphysical states because the state dependency of reflectivity is not unique. A given reflectivity value can correspond to an unlimited number of combinations of state variables involved in its calculation. Additional polarimetric radar measurements may help evaluate the performance of an analysis; therefore, the reflectivity of the horizontal polarizations ($Z_H$), differential reflectivity ($Z_{\mathrm{DR}}$), specific differential phase ($K_{\mathrm{DP}}$), and cross-correlation coefficient ($\rho_{\mathrm{hv}}$) measured by KOUN are used for verification. KOUN $V_r$ data are not used because multiple folding occurred with the data because of a low Nyquist velocity, which made unfolding difficult.

We employ a quality control procedure that is included in the ARPS package to despeckle and remove ground clutter from reflectivity data and to unfold aliased radial velocity data. Observations are interpolated to the location of the model grid horizontally, but remain on the radar elevation levels vertically (see XTD06; XJZ10). To produce the data at the analysis times at 5-min intervals, data from the same elevation at the two nearest times are interpolated to the analysis time (Tong 2006). An additional quality check is added to the polarimetric data based on the value of $\rho_{\mathrm{hv}}$; the measured $Z_{\mathrm{DR}}$ and $K_{\mathrm{DP}}$ values are flagged as bad when $\rho_{\mathrm{hv}}$ is smaller than 0.8.

## 4. Results

### a. Verification of EnKF analyses against WSR-88D observations

Figure 3 shows the differences between analyzed ensemble mean reflectivity and radial velocity from

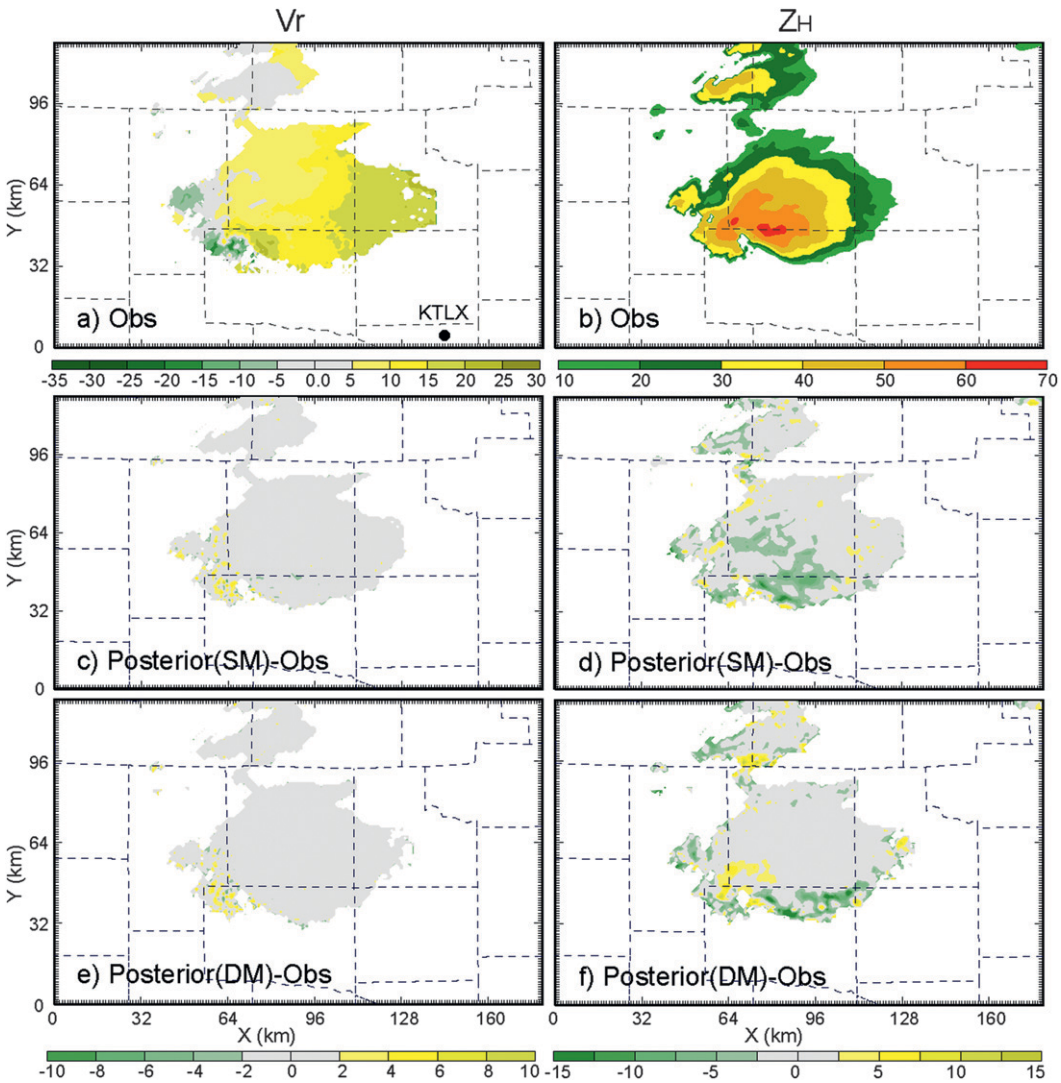


FIG. 3. KTLX observed (a) radial velocity and (b) reflectivity; (c),(d) As in (a),(b), but for posterior ensemble mean minus observation for EXP_SM at the 0.46° elevation angle valid at 0100 UTC 30 May. (e),(f) As in (c),(d), but for EXP_DM.

EXP_DM and EXP_SM at the end of the assimilation window, projected to the lowest elevation of the KTLX (0.46°), and the corresponding KTLX observations. Projection is performed to enable direct comparison. The analyzed radial velocity and reflectivity in both experiments show a good fit with observations in the shape, structure, and intensity of these fields indicated by small differences between the posterior ensemble mean and observations within the storm in general. The filter does experience some difficulty in retrieving sharp gradients in the observed values of reflectivity and radial velocity in both EXP_SM and EXP_DM. Small differences in radial velocity are found near two velocity couplets (Figs. 3c,e). Relatively larger differences in reflectivity are shown near the hook echo and in the southern edge of the forward flank (Figs. 3d,f). The filter does not perform well where the background state contains a displacement error when a sharp gradient is present because the collection of small displacement errors can lead to a less reliable covariance structure. Ensemble mean reflectivity is on average lower than observations in EXP_SM while reflectivity is slightly overestimated near the reflectivity core in EXP_DM. Still, overall differences are rather small in both fields. This degree of fit with observations is achieved at all levels (not shown). Although a good fit of the analysis to the observations in terms of the assimilated quantities is expected with a well-behaved analysis system, obtaining the results shown in Fig. 3 was

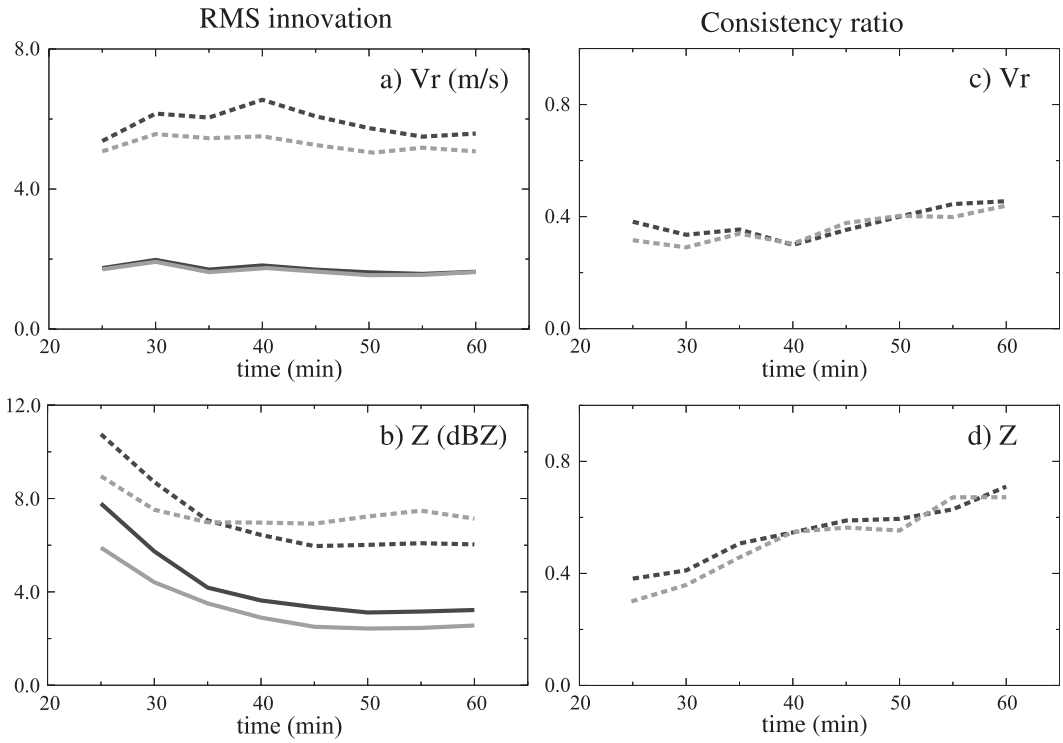


FIG. 4. The RMSIs for (a) radial velocity and (b) reflectivity for ensemble mean analyses (solid lines) and ensemble mean forecasts (dotted lines) with an SM (gray lines) and DM (black lines) scheme, and the consistency ratios for (c) radial velocity and (d) reflectivity for ensemble forecasts calculated against KTLX observations. Statistics are only computed where either observed or analyzed reflectivity is greater than 15 dB*Z*. Note that because of the overlay of curves from two experiments, we plot the analysis and forecast curves separately, instead of the often used ''sawtooth'' diagrams (e.g., Dowell et al. 2004).

not trivial when the DM scheme was used. Many experiments were performed to arrive at the ''optimal'' configuration of the EnKF system that is used in this study.

To quantitatively evaluate the performance of the EnKF analyses and forecasts, taking account of observation errors, the root-mean-square innovations (RMSI) and consistency ratios following Dowell and Wicker (2009) are averaged over the KTLX volume at each analysis time (Fig. 4). These scores are computed for all points where the observed or simulated ensemble mean reflectivity is greater than 15 dB*Z*; this criterion includes spurious echo regions in the statistics. The RMSI usually decreases rapidly within the first few cycles; therefore, we only present statistics after the fifth analysis cycle, by which time they have largely stabilized (Figs. 4a,b). The dashed curves represent the RMSI of the ensemble mean forecasts, the solid lines represent the RMSI of the ensemble mean analyses, and the black and gray curves represent EXP_DM and EXP_SM, respectively. In Fig. 4a, the 5-min velocity forecast of EXP_SM is slightly better than that of EXP_DM, while the analyzed radial velocity is nearly the same. On the other hand, the 5-min forecast reflectivity of EXP_DM is better in the later assimilation cycles, while the analyzed reflectivity of EXP_SM is consistently lower than that of EXP_DM by about 0.6 dB*Z* (Fig. 4b). In general, the RMSIs are of comparable magnitude in EXP_SM and EXP_DM during the assimilation window; the increase of innovation during forecast periods is also similar between the two. During intermediate and later cycles, the RMSIs of radial velocity decrease below 2 m $s^{-1}$ in the analyses, but quickly increase to approximately 6 m $s^{-1}$ in the 5-min forecasts. Similar behavior is seen in reflectivity when the analysis reduces the forecast RMSIs by 3–4 dB*Z*.

Another useful index that can assess the behavior of data assimilation is the consistency ratio (Dowell et al. 2004; Dowell and Wicker 2009). This value should be close to 1 when forecast ensemble variance (squared ensemble spread) is a good approximation to the forecast error variance. The consistency ratios are comparable for EXP_DM and EXP_SM, ranging from 0.3 to 0.5 for radial velocity and from 0.3 to 0.7 for reflectivity (Figs. 4c,d). While these consistency ratios are well below 1, these results are not atypical, given that underdispersion is commonly observed in real data studies

at the convective scale (Dowell and Wicker 2009; Aksoy et al. 2009). Despite the spread deficiency, the filter showed no clear sign of divergence, at least during the assimilation period examined. Additive noise was found to help maintain or increase consistency ratios with time, as indicated by the increasing trend seen in Figs. 4c,d. Efforts to further increase the consistency ratio by adding more additive noise or using a larger covariance inflation factor resulted in increased RMSIs and computational instability during the forecast in some members. Increasing observation error variance increased the ensemble spread but also RMSIs. The comparable overall diagnostics shown in Fig. 4, including the magnitude and trend of RMSIs and consistency ratios, and the supercell structure shown in Fig. 3 indicate that the two experiments are reasonably configured for our comparison purposes.

We expect a larger ensemble spread in EXP_DM than in EXP_SM, as EXP_DM has more degrees of freedom. Since we observe a faster spread reduction in EXP_DM in the observation space, we computed the ensemble spread of each model-state variable. The results indicate that in general, the three dimensionally averaged ensemble spreads of state variables in EXP_DM are consistently higher than those in EXP_SM. For example, ensemble spreads averaged over the area where $Z > 15$ dB$Z$ for $q_c$, $q_r$, $q_i$, $q_s$, and $q_h$ are $0.24 \times 10^{-2}$, $0.71 \times 10^{-2}$, $0.15 \times 10^{-2}$, $0.51 \times 10^{-2}$, and $0.72 \times 10^{-2}$ g kg$^{-1}$, respectively, at 300 s of model time but $0.28 \times 10^{-2}$, $0.75 \times 10^{-2}$, $0.81 \times 10^{-6}$, $0.36 \times 10^{-5}$, and $0.54 \times 10^{-5}$ g kg$^{-1}$, respectively, for EXP_SM. The ensemble spread of hail in EXP_SM at 300 s is almost three orders of magnitude smaller than that in EXP_DM. The same trend continues to the end of the assimilation window. Ensemble spreads of wind variables are also higher in EXP_DM than in EXP_SM. Although the spreads of the mixing ratios are generally found to be higher in EXP_DM, the combination of the mixing ratio and the total number concentration results in a smaller ensemble spread in reflectivity in DM_EXP. This is reasonable, as reflectivity is directly constrained by observations, and in the light of the fact that more degrees of freedom can be adjusted by the filter so as to better match the final solution with the observations. When this happens to all or most members, the spread can be smaller.

Because reflectivity and radial velocity data from KTLX were assimilated, a good match between the analyses and KTLX observations is expected. A much more stringent test is the fit of the analyses to independent observations. Figure 5 compares the analyzed reflectivity and radial velocity against KVNX observations that are not assimilated. The analyzed reflectivity is found to be consistent with KVNX observations (Figs. 5b,d,f), with larger differences found in the small cells north of the main storm. These cells are closer to KVNX, and therefore, KTLX observation is not available at this height. This could explain the larger differences in both reflectivity and radial velocity in those two cells (Figs. 5c–f). The differences in analyzed radial velocities are larger than those in reflectivity in the main storm (note that the two radars actually measure different components of the wind because of their differing viewing angles, while reflectivity measured by the two S-band radars is a measurement of the same quantity). For example, the differences are larger near the two small-scale cyclonic circulations found in KVNX radial velocity observations, which are labeled C1 and C2 (Fig. 5a). Two circulations are too weak and broad in the EXP_SM and EXP_DM analyses, which do not exhibit any outbound velocity in the circulation region (KVNX is located at approximately $X = 75$ km and $Y = 155$ km). Nevertheless, the radial velocity field of EXP_DM is generally better than that of EXP_SM in the high-reflectivity region where $Z > 50$ dB$Z$ within the main storm, although the size of small-scale features is still overestimated. The large error near the location of those two vortices in Fig. 5 is partly due to a small displacement of vortices with respect to KTLX. Although time interpolation was applied to get the observed radial velocity at the time of analysis, their positions are still slightly different from each other. The inbound component of analyzed wind in the northern portion of the forward flank in the main storm and in the small storm located north of the main stormis underestimated in both EXP_SM and EXP_DM. The inaccuracy of the analyzed wind in the split storm can be largely attributed to the fact that the cross-beam component of wind with respect to the KTLX radar is dominant in this region (not shown). As suggested by Dowell et al. (2004) and Tong (2006), the ensemble Kalman filter often has difficulty retrieving the cross-beam component of the wind from single Doppler radar radial velocity observations for real cases.

The vertical profiles of RMSI with respect to KVNX observations averaged over points at which observed reflectivity is greater than 15 dB$Z$ for EXP_SM (gray lines) and EXP_DM (black lines) at the end of assimilation cycles show that EXP_DM has consistently smaller RMSIs for radial velocity below the fifth elevations (Fig. 6). Between the sixth and twelfth elevations, EXP_SM displays a smaller RMSI. Above that, no reflectivity higher than 15 dB$Z$ is found. The vertical profiles at 55 min are similar to those at 60 min in EXP_SM. The larger RMSIs for reflectivity found in EXP_DM at the lower elevations are due, in part, to larger differences in the storm located north of the main storm (Fig. 5f). On the other hand, greater uncertainty in

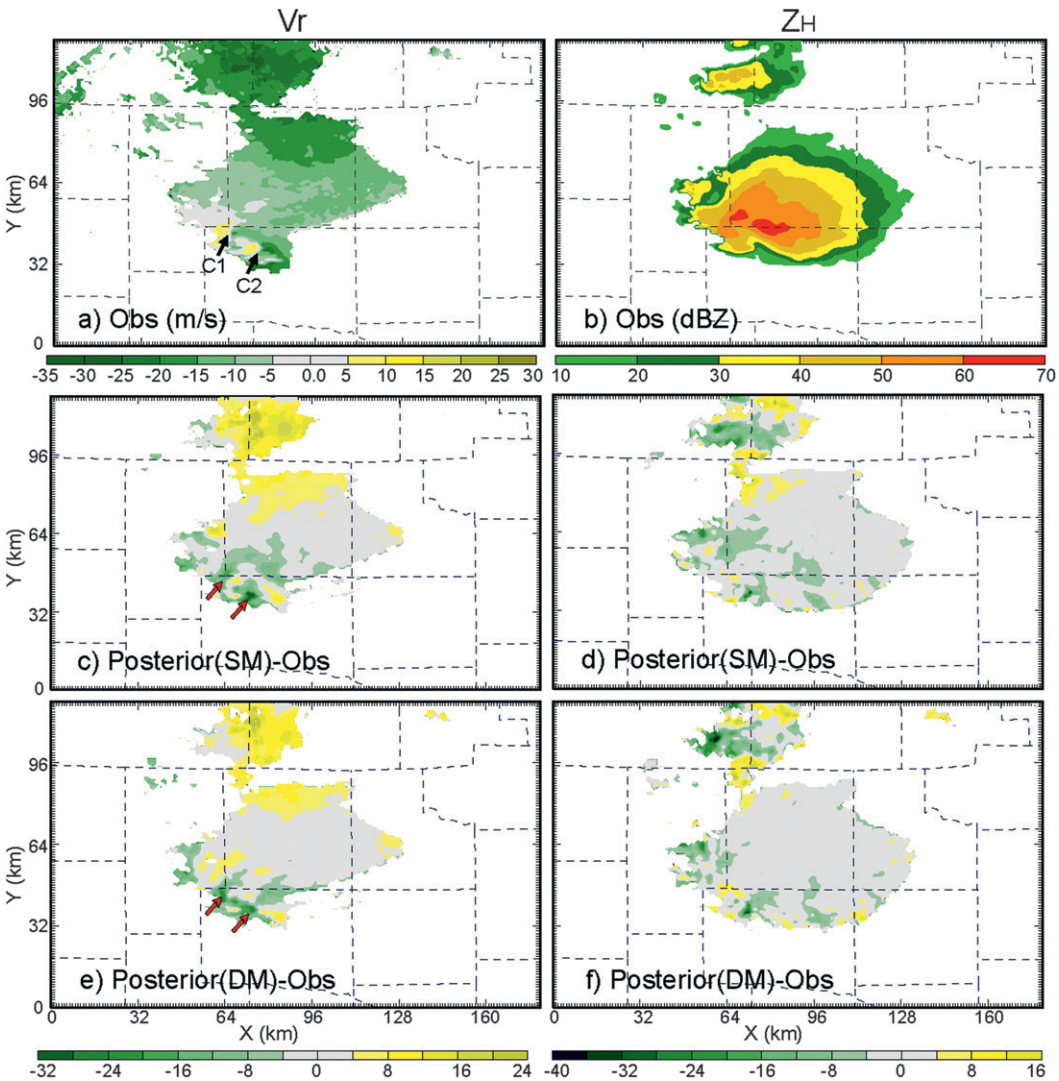


FIG. 5. As in Fig. 3, but for KVNX at the 0.5° elevation angle that provides independent observations. Two cyclonic circulations are labeled C1 and C2 and are pointed at by arrows.

$V_r$ is partly responsible for the larger RMSIs for $V_r$ at the upper levels because of the relatively larger radar resolution volume and a certain portion of missing data at 116 km and farther, which caused some issues during the dealiasing and interpolation. Nevertheless, EXP_SM and EXP_DM are generally comparable in terms of RMSIs.

At the upper levels, the analyzed reflectivity field as viewed by KTLX is still reasonably good, except near areas of high-reflectivity gradients (Figs. 7d,f). The reflectivity in the bounded weak echo region (BWER) is too high in EXP_SM (yellow area in Fig. 7d) while the intensity of the high-reflectivity wall surrounding it is underestimated in EXP_DM (larger green area in Fig. 7f). At this tilt, the analyzed radial velocity fields show relatively good agreement with the observations in both experiments, in general, except in the areas of strong inbound winds (Figs. 7c,e).

For real data experiments, diagnostics are usually performed in the observation space. Because the true state is unknown, the quality of an analysis can only be evaluated using observations. The innovation can be a useful measure of an error when an observation is a direct measurement of a state variable, such as that of pressure or wind. When the observation is an indirect measurement involving multiple state variables, such as that for radar reflectivity, interpretation of the innovation is not straightforward, as illustrated in XJZ10 for the mixing ratio and total number concentration of rain. In that study, the filter performance in identifying

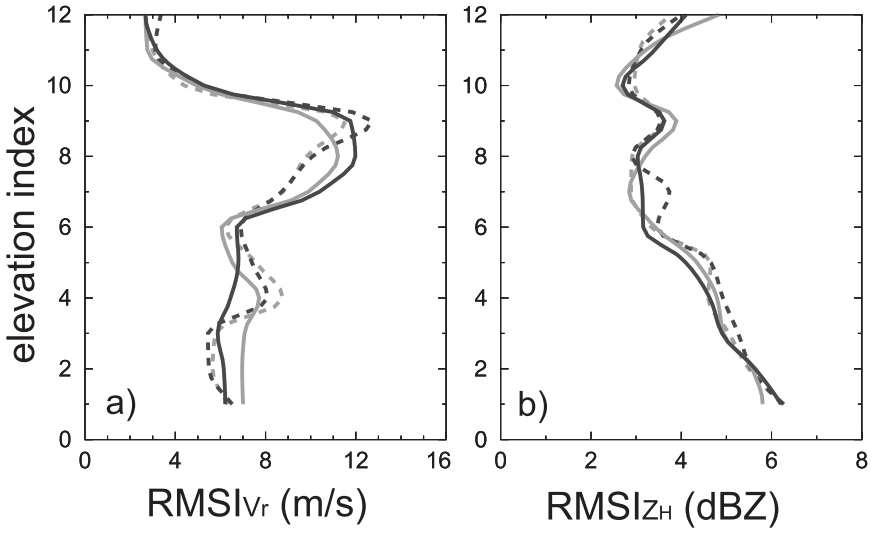


FIG. 6. The vertical profiles of RMSI of ensemble mean analyses with respect to KVNX radar for (a) radial velocity and (b) reflectivity of EXP_SM (gray lines) and EXP_DM (black lines) at 3300 s (dotted lines) and 3600 s (solid lines). RMSIs are averaged at each elevation angle over points at which the observed reflectivity is >15 dB$Z$.

correct errors in individual fields was significantly degraded when the state estimation was underconstrained by the observations. A similar problem was noted for multiple parameter estimation in Tong and Xue (2008), where the responses in terms of reflectivity to errors in different parameters can offset one another. Polarimetric radar measurements can help evaluate the quality of the analysis by providing independent information, especially information on PSDs.

### *b. Comparison with KOUN polarimetric variables*

In supercell storm simulations, PSDs of hydrometeors affect the structure, dynamics, and evolution of storms (JXZ10). Therefore, it is important for successful forecasts to properly initialize the PSDs and, at the same time, have a prediction model that is capable of accurately evolving the PSDs. The DM and TM schemes are designed to predict the evolution of PSDs, allowing different degrees of freedom within the PSD model. Verification of model PSDs is difficult, however, because of the lack of direct PSD observations, at least in three dimensions.

A number of polarimetric signatures in supercell storms and the means by which they form were documented in the observational studies of Kumjian and Ryzhkov (2008, 2009, 2010) and Romine et al. (2008). JXZ10 showed that most of these signatures could be simulated in a numerical model when a DM scheme is used even though a single sounding was used to define the storm environment. However, they reported that certain polarimetric signatures, including the $Z_{DR}$ arc and midlevel $Z_{DR}$ and $\rho_{hv}$ rings, could not be properly simulated when an SM microphysical scheme was used. Because polarimetric data and reflectivity from KOUN are not assimilated in our study, it is possible to include them as independent data for evaluating the quality of state estimation or verification. Radar scans obtained between 0058:04 and 0102:54 UTC are composited to create a 3D volume scan for KOUN. To directly compare observed and analyzed polarimetric variables, the forward observation operator described in JZX08 and Jung (2008) is utilized to convert model states into observed quantities.

In the KOUN 0.5° tilt, two reflectivity cores are found: one in the forward-flank region and one in the rear-flank region (Fig. 8a). Both reflectivity cores are reproduced quite well in EXP_SM and EXP_DM (Figs. 8b,c). A comparison of KOUN reflectivity to that from KTLX (Fig. 3b) suggested that KOUN reflectivity is about 3 dB$Z$ higher than the reflectivity of KTLX because of miscalibration. However, $Z_{DR}$ bias was found to be small and thus did not require any correction. The isolated echo east of the main storm in the KOUN data is suspected to be a second trip echo (M. Kumjian 2011, personal communication). The fact that time interpolation was not applied to the KOUN data may also be partly responsible for the reflectivity differences.

In general, the $Z_{DR}$ and $K_{DP}$ patterns in EXP_SM do not match those in the observations, despite good agreement in reflectivity. On the contrary, polarimetric signatures of EXP_DM compare favorably with $Z_{DR}$ and $K_{DP}$ patterns in the observations. The $Z_{DR}$ arc,

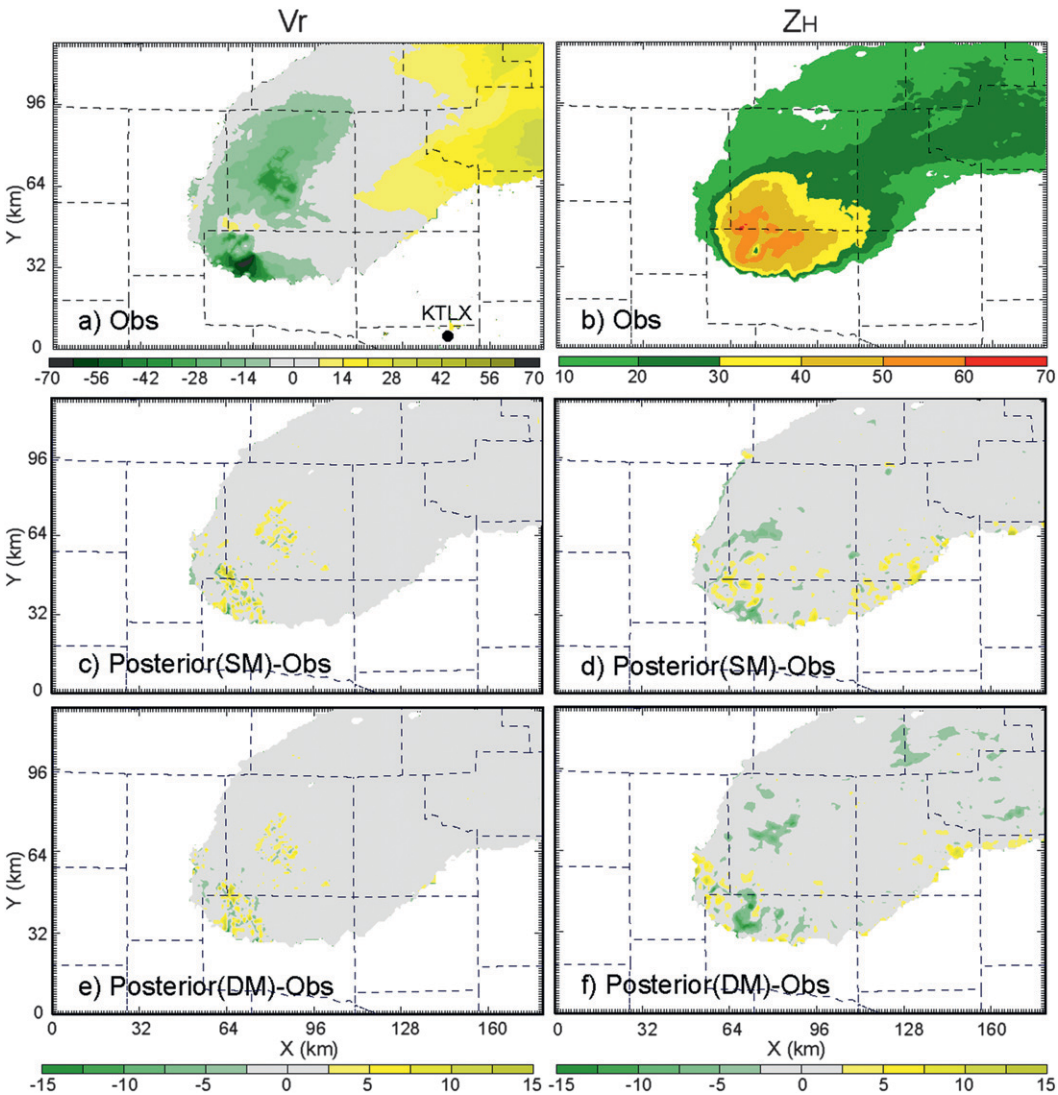


FIG. 7. As in Fig. 3, but at elevation angle of 5.11°.

a region of high $Z_{DR}$ near the surface in the southern part of the forward flank, provides evidence of a relatively high ratio of large raindrops resulting from a size-sorting mechanism (Kumjian and Ryzhkov 2008) (Fig. 8d). As shown in JXZ10, for an idealized simulation, EXP_DM is able to retrieve the $Z_{DR}$ arc signature in this real data case (Fig. 8f). The $Z_{DR}$ value in EXP_DM is generally higher than in the observations, although the peak value in the $Z_{DR}$ arc is slightly lower than in the observations. The $Z_{DR}$ maximum in EXP_DM is located north of the observed maximum, although the overall pattern suggests that the DM scheme is able to simulate the size-sorting process properly (see JXZ10 for more details). Excessive size sorting due to the fixed shape parameter is discussed in Milbrandt and Yau (2005a) and may be responsible for the rather higher $Z_{DR}$ values in the forward-flank area. This excessive size sorting may be alleviated by using a diagnostic relation for the shape parameter without increasing the number of state variables in the future. On the other hand, the $Z_{DR}$ patterns are significantly different from the observations in EXP_SM (Fig. 8e). The elongated low $Z_{DR}$ band enclosed by a dashed circle is due to the presence of hail (Fig. 9c). The $Z_{DR}$ arc is absent in EXP_SM.

Despite some observation void in the high $K_{DP}$ region, such a region is generally collocated with the region of high reflectivity, which is located north of the observed $Z_{DR}$ maximum (Fig. 8g). The analyzed $K_{DP}$ core in EXP_DM is located several kilometers northwest of the observed $K_{DP}$ core (Fig. 8i), but it is still collocated with analyzed reflectivity cores. The analyzed $K_{DP}$ cores are collocated with reflectivity in EXP_SM

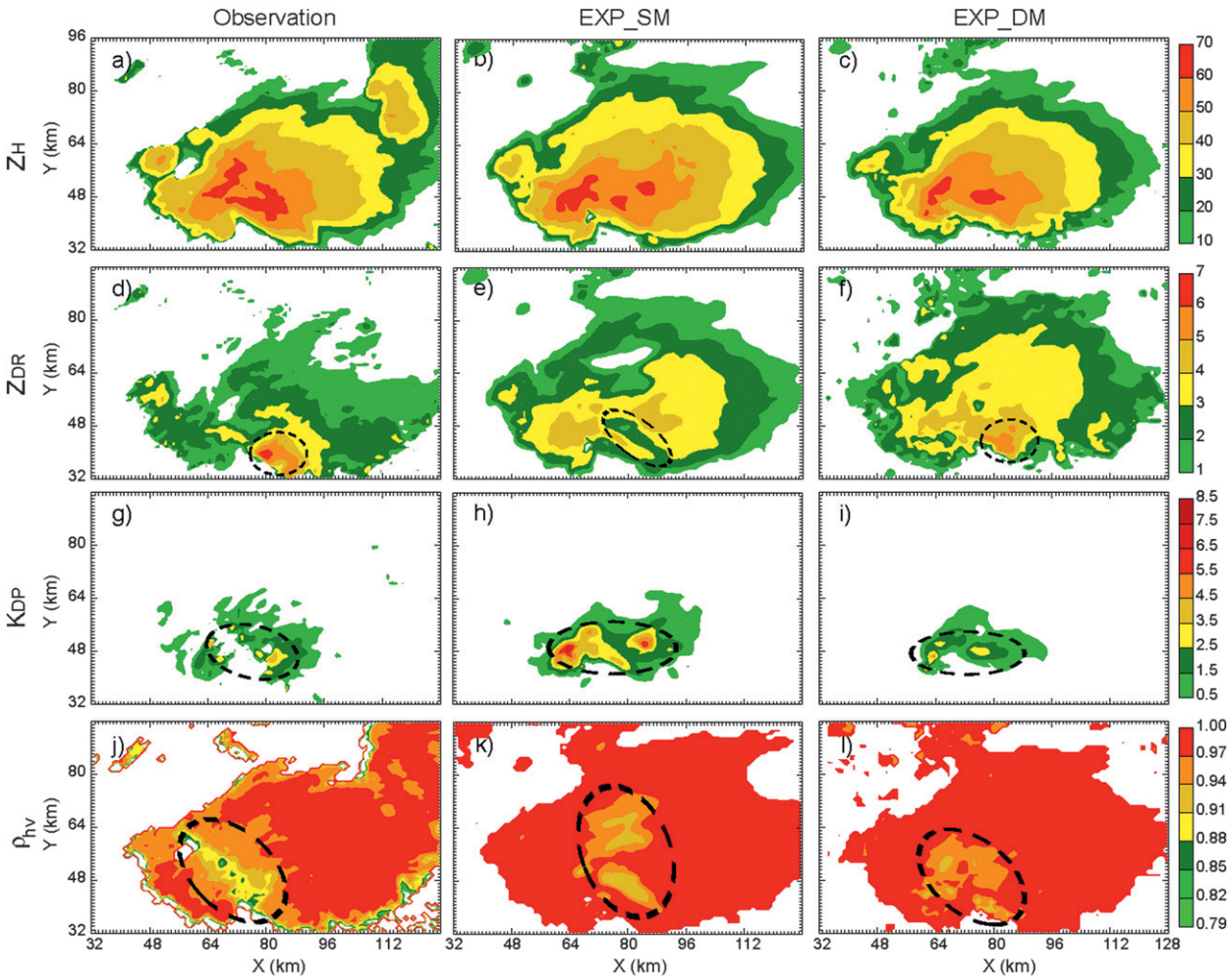


FIG. 8. (a)–(c) Reflectivity ($Z_H$; dB$Z$), (d)–(f) differential reflectivity ($Z_{DR}$; dB), and (g)–(i) differential phase ($K_{DP}$; ° km$^{-1}$). (j)–(l) Cross-correlation coefficient ($\rho_{hv}$) for the (left) KOUN, (middle) EXP_SM, and (right) EXP_DM at 0.5° tilt, valid at 0100 UTC 30 May. For EXP_SM and EXP_DM, ensemble analysis means are used to create simulated polarimetric variables at the observation points. Features of interest are enclosed by dashed circles in some panels.

(Fig. 8h), but the values are too high, partially because of the reduced rain intercept parameter. Reducing the intercept parameter increases the assumed median volume diameter of raindrops where larger drops induce a larger differential phase.

In Fig. 8j, low $\rho_{hv}$ is found in the observations in the region of inflow and to its northwest. The low $\rho_{hv}$ values at low levels can be attributed to a combination of hail and light debris carried by the inflow (Kumjian and Ryzhkov 2008). Light debris is not simulated by our prediction model or our polarimetric radar data simulator, which may explain the lack of low $\rho_{hv}$ values in the inflow region of our experiments. However, a $\rho_{hv}$ reduction around the periphery of the updraft due to hail in EXP_DM is apparent in Fig. 8l (see Fig. 9 for rainwater and hail mixing ratios). The simulated $\rho_{hv}$ of EXP_DM is generally higher than the observed value because of the simplified model of ice particles, independent treatment of each precipitating type, and lack of nonmeteorological effects within the model. Further discussion of the limitations of simulated $\rho_{hv}$ can be found in JXZ10. Therefore, simulated $\rho_{hv}$ can only be viewed qualitatively. Considering the limitations of the radar simulator, areas of $\rho_{hv}$ reduction due to meteorological factors, which are the presence of rain, hail, and a melting hail mixture, and the resonance effect of large melting hail, are found at approximately the correct locations near observed low $\rho_{hv}$ regions for EXP_DM. However, the lower $\rho_{hv}$ region is found in the forward flank, farther east and north of the observed low $\rho_{hv}$ regions, in EXP_SM, a finding that differs greatly from observations. For a more detailed discussion on how

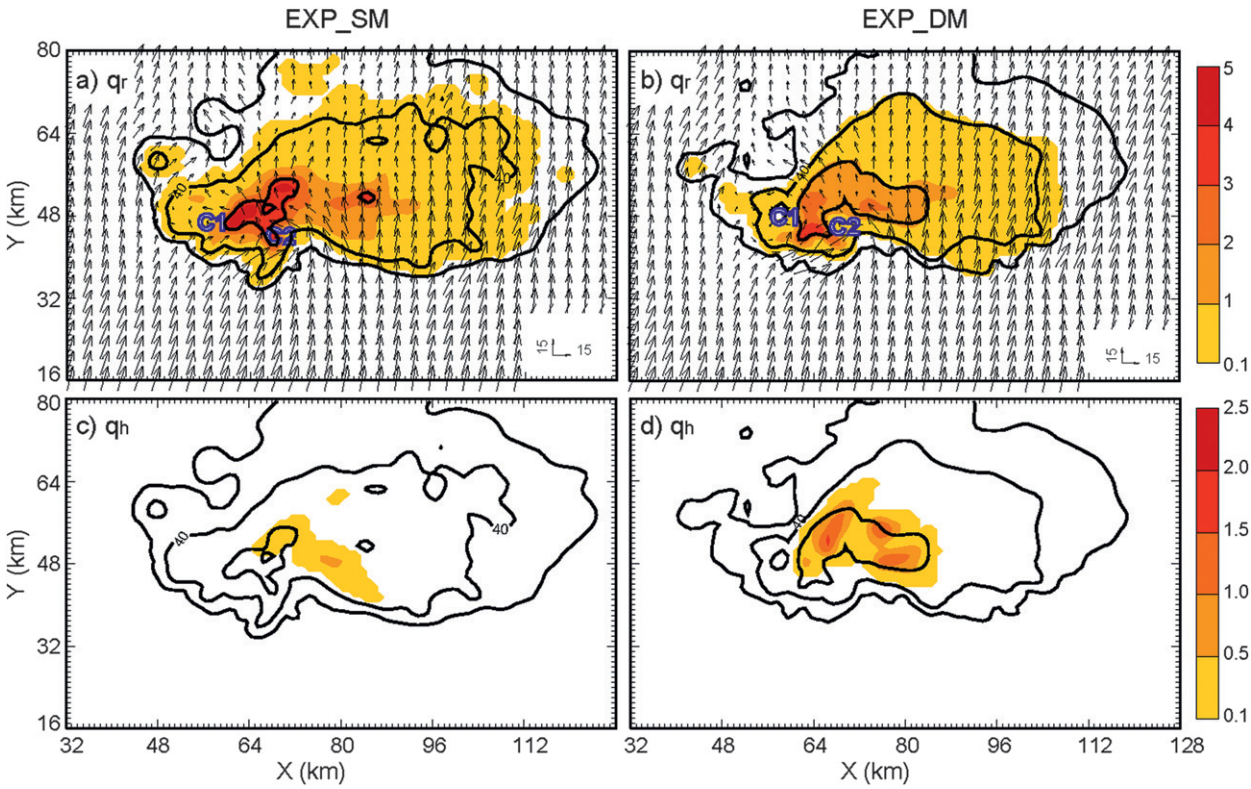


FIG. 9. (a),(b) Rainwater mixing ratio (shading; g kg$^{-1}$), horizontal wind (vectors; m s$^{-1}$), and (c),(d) hail water mixing ratio (g kg$^{-1}$) for the ensemble mean of (a),(c) EXP_SM and (b),(d) EXP_DM at 0100 UTC at $z$ = 1.5 km MSL. Reflectivity (thick solid contours at intervals of 20 dB$Z$, starting from 20 dB$Z$) is overlaid on each plot. Two cyclonic circulations from Fig. 5 are labeled C1 and C2 in (a),(b).

polarimetric signatures are simulated within a numerical model, the reader is referred to JXZ10.

### c. Comparison between EXP_SM and EXP_DM

In the previous section, we showed that the overall pattern and intensity of $Z_{DR}$, $K_{DP}$, and $\rho_{hv}$ in EXP_DM agreed relatively well with observations while EXP_SM exhibited $Z_{DR}$ and $K_{DP}$ signatures and a $\rho_{hv}$ pattern that was different than that of observations. These results indicate that the DM scheme appears to be simulating microphysical processes more accurately than the SM scheme. In this section, we compare certain model-state variables of EXP_SM and EXP_DM, emphasizing the differences in microphysical fields using the two schemes. Because of the lack of direct measurement of state variables, we have to rely on our understanding of storm dynamics, thermodynamics, and microphysics, along with polarimetric data, to help us assess the quality of the analyses.

In Fig. 9, the analyzed low-level ($z$ = 1.5 km) rainwater and hail mixing ratios at the end of the assimilation period, along with horizontal wind and reflectivity, are presented. Figure 8 showed that both EXP_SM and EXP_DM show good agreement between analyzed reflectivity and KOUN observations. The RMS difference at the end of assimilation, averaged over all grid points at which reflectivity exceeds 15 dB$Z$, is approximately 7 dB$Z$ in both experiments. That difference is higher than the RMS differences calculated against KTLX or KVNX, largely because the anomalous echo northeast of the main storm observed by KOUN, but not KTLX or KVNX.

Despite the similarity in the analyzed reflectivity, the patterns of analyzed microphysical variables vary greatly between EXP_SM and EXP_DM (Fig. 9). In both experiments, the high-reflectivity core can be attributed to the rainwater content at lower levels (Figs. 9a,b), as those cores are collocated with the area of a high rainwater mixing ratio. Hail in EXP_SM is present in a much lower amount and over a narrower area than in EXP_DM. In contrast, the hail mixing ratio is higher in EXP_DM than in EXP_SM and contributes significantly to the high reflectivity. The relatively large difference in horizontal wind at $z$ = 1.5 km above mean sea level (MSL) is found mostly in the rear-flank and inflow regions. The southerly wind in the rear-flank region and the cyclonic circulation C1 are weaker, while C2 is stronger in EXP_DM.

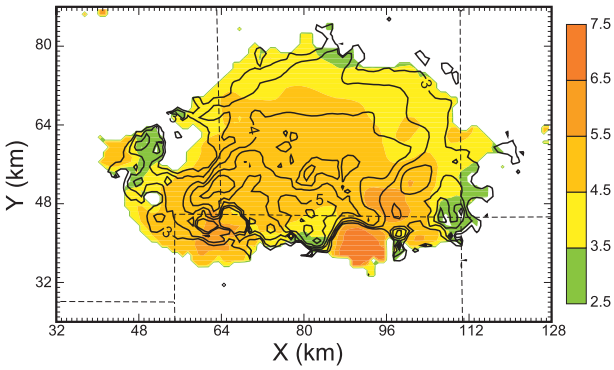


FIG. 10. Rain intercept parameter [shading; $\log_{10}(N_{0r})$] for the ensemble mean of EXP_DM at $z$ = 100 m AGL at $t$ = 3600 s of model time. Ensemble mean analysis $Z_{DR}$ (solid contours at intervals of 0.5 dB, starting from 3 dB) is overlaid. The small intercept parameter values are found in the $Z_{DR}$ arc.

The difference between the SM and DM schemes is obvious from the rain intercept parameters, $N_{0r}$, computed from EXP_DM (Fig. 10) at $z$ = 100 m above ground level (AGL), where the rain intercept parameter used in EXP_SM is $\log(8.0 \times 10^5) = 5.9$. The $\log(N_{0r})$ values are smaller than 5.5 in most areas in EXP_DM. This implies that the raindrops would be larger than those in EXP_SM for the same rainwater mixing ratio. The lower intercept parameters collocated with the area with high $Z_{DR}$ values in the $Z_{DR}$ arc suggests that large raindrops are responsible for this signature in EXP_DM.

Although the intercept parameter computed from EXP_DM displays the PSD shifts toward smaller or larger drops compared to the SM results, it is not an absolute measure of the particle size. Figure 11 shows the mean-mass diameter [see Eq. (8) of JXZ10] of raindrops at $z$ = 2 km and hailstones at $z$ = 6 km along with their mixing ratios. In EXP_SM, the particle size is a monotonic function of its mixing ratio. Therefore, large drops exist only in the areas with a high mixing ratio, as shown in Figs. 11a,c. In Figs. 11b,d, it is clear that raindrops are indeed larger in EXP_DM than in EXP_SM in the high-reflectivity regions at the lower levels. In contrast to EXP_SM, the smaller size of hailstones is associated with a higher hail mixing ratio in EXP_DM. The mismatch between the hail mixing ratio contours and hailstone size shading in the forward flank suggests that a smaller number of large hailstones exist in the vicinity of updrafts, while a large number of smaller hailstones are being carried away.

The distribution of hydrometeors at $z$ = 8 km also differs greatly between EXP_SM and EXP_DM (Fig. 12), similar to the results seen in Fig. 9. In EXP_SM, the amounts of hail and snow are comparable where $Z_H >$ 40 dB$Z$ at this height, with hail contributing significantly

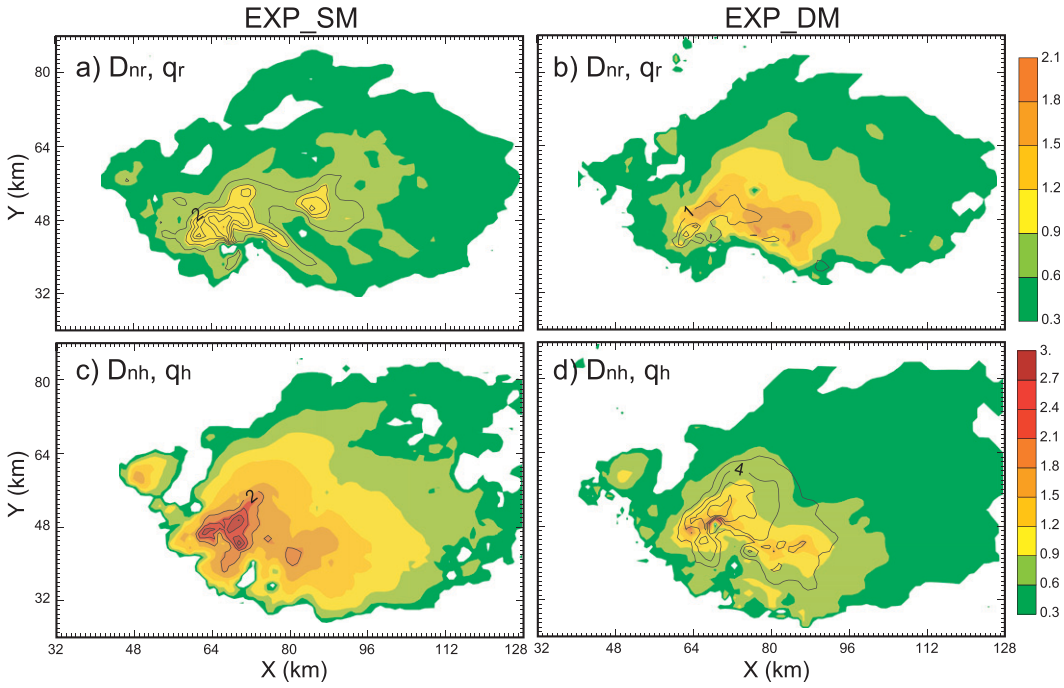


FIG. 11. Mean-mass diameters (shading; mm) of (a),(b) raindrops at $z$ = 2.5 km and (c),(d) hailstones at $z$ = 6 km MSL computed from the ensemble mean analysis for (a),(c) EXP_SM and (b),(d) EXP_DM at 0100 UTC. (a),(c) Rainwater mixing ratio (solid contours at intervals of 1.0 g kg$^{-1}$, starting from 1.0 g kg$^{-1}$) and (b),(d) hail water mixing ratio (solid contours at intervals of 2.0 g kg$^{-1}$, starting from 2.0 g kg$^{-1}$) is overlaid on each plot.

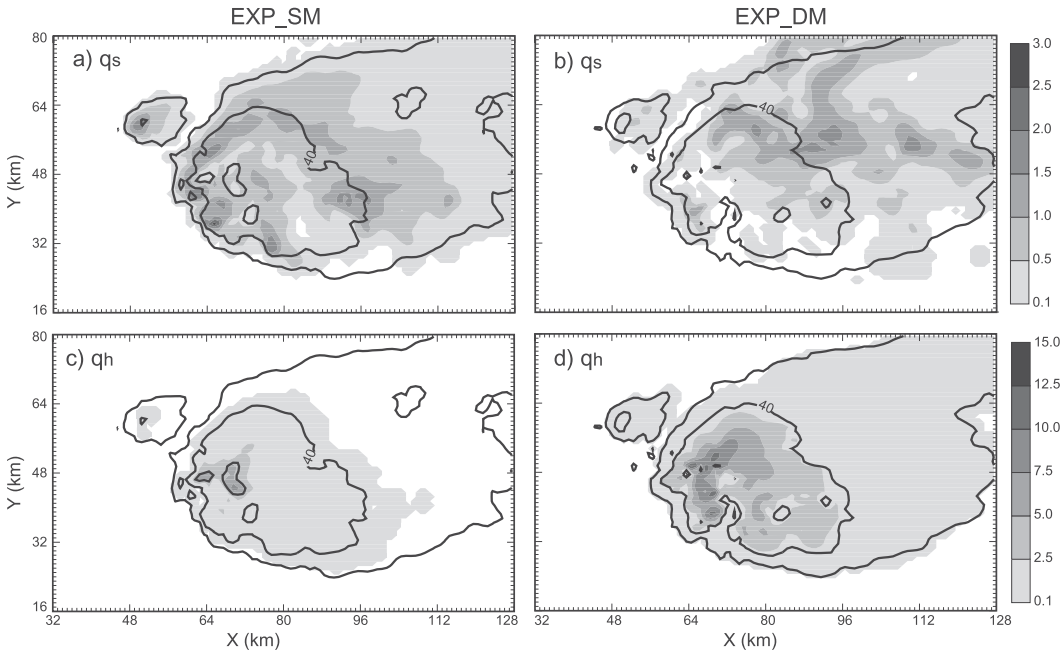


FIG. 12. (a),(b) Snow water mixing ratio (shading; g kg$^{-1}$) and (c),(d) hail water mixing ratio (g kg$^{-1}$) for the ensemble mean of (a),(c) EXP_SM and (b),(d) EXP_DM at 0100 UTC at $z$ = 8 km MSL. Reflectivity (thick solid contours at intervals of 20 dB$Z$, starting from 20 dB$Z$) is overlaid on each plot.

to the reflectivity maximum. The localized high hail content found in the vicinity of updrafts can be attributed to the large size assumption in the SM scheme. However, in EXP_DM, hail is dominant in a much wider area, where $Z_H > 40$ dB$Z$ while the snow content increases downstream. This is reasonable because the hailstones can be much smaller to represent growing ice particles by riming in EXP_DM, as shown in Fig. 11. Without in situ observations, it is difficult to say with certainty how good or bad those state estimates are. However, a high concentration of hail in EXP_DM is shown in the updraft region, which is inferred from the location of BWER, with a main region of hail growth to the left of the updraft (e.g., Miller et al. 1988). The maximum mean-mass diameter of the hail at this level is approximately 2.1 mm in EXP_DM.

Weygandt et al. (2002) and Dowell et al. (2004, 2011) found it difficult to retrieve low-level features, such as the cold pool, from radar data. This can be partly attributed to the lack of radar data near the surface because of the earth curvature effect and model errors associated with resolution and model physics. Furthermore, Dowell et al. (2011) demonstrated that the perturbation temperature near the surface is very sensitive to the reflectivity data assimilation algorithm and to the ensemble spread in temperature, suggesting low confidence in the analyzed cold pool. In fact, the SM and DM experiments show somewhat different low-level features, but the results are inconclusive given the lack of observations near the surface, so they are not shown here.

## 5. Summary and discussion

Supercell thunderstorms are known to exhibit many distinct polarimetric signatures that are associated with size distributions, shapes, phase composition, and orientations of particles that exhibit large natural variability within a storm as a result of storm dynamics and microphysics. Use of a single-moment (SM) microphysics scheme substantially limits the capability of a numerical weather prediction model to simulate the observed variability in particle size distributions (PSDs) for supercell storms, although such schemes are widely used primarily because of their lower computational costs. Two- or higher-moment microphysics schemes, on the other hand, are capable of simulating observed PSD variability to a certain extent. However, some issues need to be addressed, including increased computational cost, introduction of new uncertainties into the microphysics parameterization, and a more seriously underconstrained situation within model-state estimation due to an increased degree of freedom. In this paper, an effort was made to address the latter issue with a real thunderstorm case using an ensemble Kalman filter (EnKF) method.

The 29–30 May 2004 central Oklahoma tornado outbreak case is selected to investigate the ability of EnKF to estimate state variables that are associated with a double-moment (DM) microphysics scheme. The analysis results are then compared with those obtained using a single-moment (SM) scheme and verified against data from WSR-88Ds at Oklahoma City (KLTX) and Vance Air Force Base (KVNX), as well as data from an experimental polarimetric WSR-88D in Norman, Oklahoma (KOUN). The analyzed reflectivity fields from the experiments using SM and DM schemes (EXP_SM and EXP_DM, respectively) compare well in general with observed reflectivity, both for observations that are assimilated and observations from independent radars. When projected to the radial directions of KVNX, the analyzed velocity field exhibits rather large differences from KVNX observations of radial velocity, which were not assimilated. This is likely associated with difficulties in retrieving the cross-beam component of the wind from a single radar. Nonetheless, the radial velocity field of EXP_DM matches slightly better with KVNX observations, at least at the lower levels, than that of EXP_SM. Although EXP_SM exhibits smaller RMSIs at the upper levels, the result is less trustworthy because of larger uncertainties due to large resolution volume and some missing data in the KVNX observations used for verification.

Polarimetric data can be very useful in the verification of convective-scale modeling studies because they contain additional information on the properties of hydrometeors, including their PSD, shape, phase composition, and orientation. A comparison between simulated polarimetric variables from the analyses and the corresponding observations revealed that the analyzed $Z_{DR}$ is missing a key signature of a supercell storm and that $K_{DP}$ values are too high in the experiment using an SM scheme, despite good agreement in reflectivity. On the contrary, polarimetric signatures in the experiment using a DM scheme compare rather well with observations in terms of the general shape, location, and intensity of the signatures.

Although the analyzed reflectivity fields in EXP_SM and EXP_DM are comparable, the dominant form of hydrometeor species in the analyses is different at both the lower and upper levels. Near the surface where snow is absent, EXP_DM produces more hail than EXP_SM, which significantly contributes to the reflectivity maxima. At the upper levels where rainwater is absent, hail is dominant in EXP_DM, while snow dominates in EXP_SM.

A set of experiments has been performed using the MY SM scheme during our study. However, the high hail bias present in the MY scheme is aggravated by reflectivity assimilation and leads to an even larger hail bias. Therefore, we did not present the results here. We concluded that more sensitivity experiments may be needed for that scheme.

The results of this study indicate that a properly designed EnKF system based on a DM microphysics scheme is able to estimate the increased number of microphysical fields associated with the scheme reasonably well for a real data case, even in the presence of significant uncertainties from many sources. In fact, the model DSDs agree better with DSDs inferred from the polarimetric signatures of a supercell when using a DM rather than an SM scheme; that is large raindrops in the southern edge of the forward flank near the surface and a large number of small hailstones or graupel around updrafts at the upper levels. We realize that the conclusions made here are based on a single real data case; therefore, more robust conclusions require the investigation of many additional cases. As the first attempt to examine the ability of an EnKF data assimilation system to correctly analyze polarimetric signatures using a DM microphysics scheme, we believe that many of the findings in this study are very meaningful.

*Acknowledgments.* The authors thank Louis Wicker for his helpful comments and Nathan Snook for proofreading. The authors also thank Matthew Kumjian for helpful discussions on the KOUN data quality issue. This work was primarily supported by NSF Grant EEC-0313747. Supplementary support was also provided by NSF Grants AGS-0802888, AGS-0608168, AGS-0750790, OCI-0905040, and NOAA Warn-on-Forecast Grant NA080AR4320904. The computations were performed at the OU Supercomputing Center for Education and Research (OSCER) and OSCER Director Henry Neeman provided valuable technical expertise. Supercomputing resources at the Pittsburgh Supercomputing Center and the National Center for Supercomputing Applications were also used.

## REFERENCES

Aksoy, A., D. C. Dowell, and C. Snyder, 2009: A multicase comparative assessment of the ensemble Kalman filter for assimilation of radar observations. Part I: Storm-scale analyses. *Mon. Wea. Rev.,* **137,** 1805–1824.

Anderson, J. L., 2001: An ensemble adjustment Kalman filter for data assimilation. *Mon. Wea. Rev.,* **129,** 2884–2903.

Barker, D. M., W. Huang, Y.-R. Guo, and A. Bourgeois, 2003: A three-dimensional variational (3DVAR) data assimilation system for use with MM5. NCAR Tech. Note NCAR/TN-453 1 STR, 68 pp. [Available from UCAR Communications, P.O. Box 3000, Boulder, CO 80307.]

Bishop, C. H., B. J. Etherton, and S. J. Majumdar, 2001: Adaptive sampling with the ensemble transform Kalman filter. Part I: Theoretical aspects. *Mon. Wea. Rev.,* **129,** 420–436.

Bluestein, H. B., M. M. French, and R. L. Tanamachi, 2007: Close-range observations of tornadoes in supercells made with

a dual-polarization, X-band, mobile Doppler radar. *Mon. Wea. Rev.,* **135,** 1522–1543.

Burgers, G., P. J. van Leeuwen, and G. Evensen, 1998: Analysis scheme in the ensemble Kalman filter. *Mon. Wea. Rev.,* **126,** 1719–1724.

Cotton, W. R., G. J. Tripoli, R. M. Rauber, and E. A. Mulvihill, 1986: Numerical simulation of the effects of varying ice crystal nucleation rates and aggregation processes on orographic snowfall. *J. Climate Appl. Meteor.,* **25,** 1658–1680.

Dawson, D. T., II, M. Xue, J. A. Milbrandt, and M. K. Yau, 2010: Comparison of evaporation and cold pool development between single-moment and multimoment bulk microphysics schemes in idealized simulations of tornadic thunderstorms. *Mon. Wea. Rev.,* **138,** 1152–1171.

——, L. J. Wicker, E. R. Mansell, and R. L. Tanamachi, 2012: Impact of the environmental low-level wind profile on ensemble forecasts of the 4 May 2007 Greensburg, Kansas, tornadic storm and associated mesocyclones. *Mon. Wea. Rev.,* **140,** 696–716.

Dowell, D. C., and L. J. Wicker, 2009: Additive noise for storm-scale ensemble data assimilation. *J. Atmos. Oceanic Technol.,* **26,** 911–927.

——, F. Zhang, L. J. Wicker, C. Snyder, and N. A. Crook, 2004: Wind and temperature retrievals in the 17 May 1981 Arcadia, Oklahoma supercell: Ensemble Kalman filter experiments. *Mon. Wea. Rev.,* **132,** 1982–2005.

——, L. J. Wicker, and C. Snyder, 2011: Ensemble Kalman filter assimilation of radar observations of the 8 May 2003 Oklahoma City supercell: Influences of reflectivity observations on storm-scale analysis. *Mon. Wea. Rev.,* **139,** 272–294.

Ebisuzaki, W., and E. Kalnay, 1991: Ensemble experiments with a new lagged analysis forecasting scheme. Research Activities in Atmospheric and Oceanic Modeling Rep. 15, WMO, 423 pp.

Evensen, G., 1994: Sequential data assimilation with a nonlinear quasi-geostrophic model using Monte Carlo methods to forecast error statistics. *J. Geophys. Res.,* **99,** 10 143–10 162.

——, 2003: The ensemble Kalman filter: Theoretical formulation and practical implementation. *Ocean Dyn.,* **53,** 343–367.

——, and P. J. van Leeuwen, 1996: Assimilation of *Geosat* altimeter data for the Agulhas current using the ensemble Kalman filter with a quasigeostrophic model. *Mon. Wea. Rev.,* **124,** 85–96.

Ferrier, B. S., 1994: A double-moment multiple-phase four-class bulk ice scheme. Part I: Description. *J. Atmos. Sci.,* **51,** 249–280.

——, W.-K. Tao, and J. Simpson, 1995: A double-moment multiple-phase four-class bulk ice scheme. Part II: Simulations of convective storms in different large-scale environments and comparisons with other bulk parameterizations. *J. Atmos. Sci.,* **52,** 1001–1033.

Gaspari, G., and S. E. Cohn, 1999: Construction of correlation functions in two and three dimensions. *Quart. J. Roy. Meteor. Soc.,* **125,** 723–757.

Hou, D., E. Kalnay, and K. K. Droegemeier, 2001: Objective verification of the SAMEX '98 ensemble forecasts. *Mon. Wea. Rev.,* **129,** 73–91.

Houtekamer, P. L., and H. L. Mitchell, 1998: Data assimilation using an ensemble Kalman filter technique. *Mon. Wea. Rev.,* **126,** 796–811.

Hu, M., 2005: 3DVAR and cloud analysis with WSR-88D level-II data for the prediction of tornadic thunderstorms. Ph.D. dissertation, School of Meteorology, University of Oklahoma, 217 pp.

Huang, X.-Y., 2000: Variational analysis using spatial filters. *Mon. Wea. Rev.,* **128,** 2588–2600.

Jung, Y., 2008: State and parameter estimation using polarimetric radar data and an ensemble Kalman filter. Ph.D. dissertation, School of Meteorology, University of Oklahoma, 209 pp.

——, G. Zhang, and M. Xue, 2008a: Assimilation of simulated polarimetric radar data for a convective storm using ensemble Kalman filter. Part I: Observation operators for reflectivity and polarimetric variables. *Mon. Wea. Rev.,* **136,** 2228–2245.

——, M. Xue, G. Zhang, and J. Straka, 2008b: Assimilation of simulated polarimetric radar data for a convective storm using ensemble Kalman filter. Part II: Impact of polarimetric data on storm analysis. *Mon. Wea. Rev.,* **136,** 2246–2260.

——, ——, and ——, 2010: Simulations of polarimetric radar signatures of a supercell storm using a two-moment bulk microphysics scheme. *J. Appl. Meteor. Climatol.,* **49,** 146–163.

Koenig, L. R., and F. W. Murray, 1976: Ice-bearing cumulus cloud evolution: Numerical simulation and general comparison against observations. *J. Appl. Meteor.,* **15,** 747–762.

Kong, F., K. K. Droegemeier, and N. L. Hickmon, 2006: Multiresolution ensemble forecasts of an observed tornadic thunderstorm system. Part I: Comparison of coarse- and fine-grid experiments. *Mon. Wea. Rev.,* **134,** 807–833.

Kumjian, M. R., and A. V. Ryzhkov, 2008: Polarimetric signatures in supercell thunderstorms. *J. Appl. Meteor. Climatol.,* **47,** 1940–1961.

——, and ——, 2009: Storm-relative helicity revealed from polarimetric radar measurements. *J. Atmos. Sci.,* **66,** 667–685.

——, and ——, 2010: The impact of evaporation on polarimetric characteristics of rain: The theoretical model and practical implications. *J. Appl. Meteor. Climatol.,* **49,** 1247–1267.

Lin, Y.-L., R. D. Farley, and H. D. Orville, 1983: Bulk parameterization of the snow field in a cloud model. *J. Climate Appl. Meteor.,* **22,** 1065–1092.

Liu, H., and M. Xue, 2006: Retrieval of moisture from slant-path water vapor observations of a hypothetical GPS network using a three-dimensional variational scheme with anisotropic background error. *Mon. Wea. Rev.,* **134,** 933–949.

MacGorman, D. R., and Coauthors, 2008: TELEX: The Thunderstorm Electrification and Lightning Experiment. *Bull. Amer. Meteor. Soc.,* **89,** 997–1013.

Meyers, M. P., R. L. Walko, J. R. Harrington, and W. R. Cotton, 1997: New RAMS cloud microphysics parameterization. Part II: The two-moment scheme. *Atmos. Res.,* **45,** 3–39.

Milbrandt, J. A., and M. K. Yau, 2005a: A multimoment bulk microphysics parameterization. Part I: Analysis of the role of the spectral shape parameter. *J. Atmos. Sci.,* **62,** 3051–3064.

——, and ——, 2005b: A multimoment bulk microphysics parameterization. Part II: A proposed three-moment closure and scheme description. *J. Atmos. Sci.,* **62,** 3065–3081.

——, and ——, 2006: A multimoment bulk microphysics parameterization. Part IV: Sensitivity experiments. *J. Atmos. Sci.,* **63,** 3137–3159.

Miller, L. J., J. D. Tuttle, and C. A. Knight, 1988: Airflow and hail growth in a severe northern High Plains supercell. *J. Atmos. Sci.,* **45,** 736–762.

Morrison, H., J. A. Curry, and V. I. Khvorostyanov, 2005: A new double-moment microphysics parameterization for application in cloud and climate models. Part I: Description. *J. Atmos. Sci.,* **62,** 1665–1677.

Purser, R. J., W.-S. Wu, D. F. Parrish, and N. M. Roberts, 2003: Numerical aspects of the application of recursive filters to variational statistical analysis. Part II: Spatially inhomogeneous and anisotropic general covariances. *Mon. Wea. Rev.,* **131,** 1536–1548.

Romine, G. S., D. W. Burgess, and R. B. Wilhelmson, 2008: A dual-polarization-radar-based assessment of the 8 May 2003 Oklahoma City area tornadic supercell. *Mon. Wea. Rev.,* **136,** 2849–2870.

Snook, N., and M. Xue, 2008: Effects of microphysical drop size distribution on tornadogenesis in supercell thunderstorms. *Geophys. Res. Lett.,* **35,** L24803, doi:10.1029/2008GL035866.

Snyder, C., and F. Zhang, 2003: Assimilation of simulated Doppler radar observations with an ensemble Kalman filter. *Mon. Wea. Rev.,* **131,** 1663–1677.

Tippett, M. K., J. L. Anderson, C. H. Bishop, T. M. Hamill, and J. S. Whitaker, 2003: Ensemble square root filters. *Mon. Wea. Rev.,* **131,** 1485–1490.

Tong, M., 2006: Ensemble Kalman filter assimilation of Doppler radar data for the initialization and prediction of convective storms. Ph.D. dissertation, School of Meteorology, University of Oklahoma, 243 pp.

——, and M. Xue, 2005: Ensemble Kalman filter assimilation of Doppler radar data with a compressible nonhydrostatic model: OSS experiments. *Mon. Wea. Rev.,* **133,** 1789–1807.

——, and ——, 2008: Simultaneous estimation of microphysical parameters and atmospheric state with simulated radar data and ensemble square root Kalman filter. Part II: Parameter estimation experiments. *Mon. Wea. Rev.,* **136,** 1649–1668.

Ulbrich, C. W., 1983: Natural variations in the analytical form of the raindrop size distribution. *J. Climate Appl. Meteor.,* **22,** 1204–1215.

Vivekanandan, J., W. M. Adams, and V. N. Bringi, 1991: Rigorous approach to polarimetric radar modeling of hydrometeor orientation distributions. *J. Appl. Meteor.,* **30,** 1053–1063.

Waterman, P. C., 1969: Scattering by dielectric obstables. *Alta Freq.,* **38** (Special Edition), 348–352.

Weygandt, S. S., A. Shapiro, and K. K. Droegemeier, 2002: Retrieval of model initial fields from single-Doppler observations of a supercell thunderstorm. Part II: Thermodynamic retrieval and numerical prediction. *Mon. Wea. Rev.,* **130,** 454–476.

Whitaker, J. S., and T. M. Hamill, 2002: Ensemble data assimilation without perturbed observations. *Mon. Wea. Rev.,* **130,** 1913–1924.

Xue, M., K. K. Droegemeier, and V. Wong, 2000: The Advanced Regional Prediction System (ARPS)—A multiscale nonhydrostatic atmospheric simulation and prediction tool. Part I: Model dynamics and verification. *Meteor. Atmos. Phys.,* **75,** 161–193.

——, and Coauthors, 2001: The Advanced Regional Prediction System (ARPS)—A multiscale nonhydrostatic atmospheric simulation and prediction tool. Part II: Model physics and applications. *Meteor. Atmos. Phys.,* **76,** 143–165.

——, D.-H. Wang, J.-D. Gao, K. Brewster, and K. K. Droegemeier, 2003: The Advanced Regional Prediction System (ARPS), storm-scale numerical weather prediction and data assimilation. *Meteor. Atmos. Phys.,* **82,** 139–170.

——, M. Tong, and K. K. Droegemeier, 2006: An OSSE framework based on the ensemble square root Kalman filter for evaluating impact of data from radar networks on thunderstorm analysis and forecast. *J. Atmos. Oceanic Technol.,* **23,** 46–66.

——, Y. Jung, and G. Zhang, 2010: State estimation of convective storms with a two-moment microphysics scheme and an ensemble Kalman filter: Experiments with simulated radar data. *Quart. J. Roy. Meteor. Soc.,* **136,** 685–700.

Ziegler, C. L., 1985: Retrieval of thermal and microphysical variables in observed convective storms. Part I: Model development and preliminary testing. *J. Atmos. Sci.,* **42,** 1487–1509.